Asian Journal of Chemistry; Vol. 38, No. 1 (2026), 141-152
ASIAN JOURNAL OF CHEMISTRY
https://doi.org/10.14233/ajchem.2026.34899

Synthesis and Comprehensive Characterisation of Pure SnO_2 Nanoparticles: Insights into Photocatalytic Activity and Electrochemical Performance

T. NESAVI[1], L. BALU[1,2,*], R. EZHIL PAVAI[1,3] and M. AJITH KUMAR[4]

[1]Department of Physics, Annamalai University, Annamalai Nagar-608002, India
[2]Department of Physics, Government Arts College, C. Mutlur, Chidambaram-608102, India
[3]Department of Physics, Thiru Kolanjiappar Government Arts College, Virudhachalam-606001, India
[4]Department of Chemistry (S&H), Loyola Institute of Technology, Palanchur, Chennai-600123, India

*Corresponding author: E-mail: balu77ezhil@gmail.com

Received: 16 September 2025 *Accepted*: 15 November 2025 *Published online*: 31 December 2025 AJC-22232

Tin oxide nanoparticles (SnO_2 NPs) were synthesized *via* a straightforward hydrothermal approach and subsequently annealed at temperatures of 500 ºC, 600 ºC and 700 ºC. Comprehensive characterisation of these nanoparticles was performed using X-ray diffraction (XRD), Fourier-transform infrared spectroscopy (FTIR), field emission scanning electron microscopy with energy-dispersive X-ray spectroscopy (FESEM-EDS), high-resolution transmission electron microscopy with selected area electron diffraction (HRTEM-SAED), UV-visible diffuse reflectance spectroscopy (UV-DRS) and X-ray photoelectron spectroscopy (XPS). XRD patterns revealed a tetragonal crystal structure, with the average crystallite size increasing from 8 nm to 28 nm as the annealing temperature was raised, a finding that was corroborated by TEM analysis. FTIR spectroscopy confirmed the presence of Sn–O–Sn bonds, indicated by absorption peaks at 644 cm^{-1}. FESEM analysis showed a predominantly spherical morphology and EDX spectra verified the presence of tin and oxygen. The optical band gap of Sn7 NPs was determined to be 3.43 eV through UV-DRS using the Kubelka–Munk method. XPS analysis provided insights into the electronic structure and confirmed the phase purity and elemental composition of the samples. The SnO_2 (Sn7) electrode delivered a specific capacitance of 271 F g^{-1} at a current density of 0.2 A g^{-1} and exhibited remarkable cyclic stability, retaining 86.14% of their capacitance after 2000 cycles. Furthermore, the photocatalytic activity of Sn7 catalyst was assessed under sunlight, revealing a notable 85% degradation of methyl violet dye. These findings highlight the dual functionality of nanosized SnO_2, making it a promising material for both energy storage and environmental applications.

Keywords: Hydrothermal method, SnO_2 NPs, Photocatalytic behaviour, Supercapacitor.

INTRODUCTION

Over the past decade, metal oxide semiconductors have emerged as a highly significant class of materials due to their unique physical, chemical and thermal properties. These characteristics have led to their widespread application across various scientific and technological domains [1]. Notable examples of metal oxides include MnO_2, TiO_2, V_2O_5, Fe_2O_3, CdO, ZnO, Bi_2O_3, ZrO_2 and SnO_2. Among these, SnO_2 stands out as a prominent n-type semiconductor (E_g = 3.6 eV at bulk state) owing to its exceptional electrical conductivity, chemical stability, high carrier density and oxygen vacancy. This makes SnO_2 highly valuable for a range of applications, including transparent electrodes in dye-sensitized solar cells, gas sensors, supercapacitors, photocatalysts and lithium-ion batteries [2-4]. Its distinctive structure and robust catalytic properties make SnO_2 a focal point of research for both electrochemical and photocatalytic applications [5]. SnO_2 in particular, is a promising candidate for energy conversion and storage due to its superior optical and electrical properties, an optimal bandgap of (3.6 eV) and significant electrochemical activity. Moreover, its cost-effectiveness, non-toxicity and high thermal and chemical stability further enhance its appeal for these applications [6]. Tin dioxide (SnO_2), a metal oxide semiconductor, has been widely applied in photocatalysis due to some of its excellent properties such as high electroconductibility and relatively low cost. It can be used to fabricate composite photocatalysts and then enhance the separation efficiency of the photogenerated carrier of other semiconductors [7].

Supercapacitors (SCs), also known as ultracapacitors or electrochemical capacitors, have gained considerable attention in the quest for sustainable energy solutions due to their superior attributes, including extended lifespan, high power density and substantial energy density. They outperform various electrical energy storage devices such as Faradic batteries, electrostatic capacitors, ceramic capacitors and electrolytic capacitors [8]. SCs are categorized based on their energy storage mechanisms into electrical double-layer capacitors (EDLCs) and pseudo-capacitors. EDLCs store energy through the accumulation of electrical and ionic charges at the electrode-electrolyte interface, a non-Faradic process typically associated with carbon-based materials. Enhanced electrochemical performance in these capacitors is attributed to the surface area and porosity of the electrode materials, which include conducting polymers, carbon and transition metal oxides [9]. In contrast, pseudo-capacitors, which generally offer higher specific capacitance and energy density compared to EDLCs, use metal oxides as electron-active materials in their electrodes [10].

In recent times, the disposal of synthetic dyes and pigments from industries such as textiles, food processing, paper, leather and printing has posed significant environmental challenges. These dyes, which are often toxic, contaminate water bodies and disrupt aquatic ecosystems by blocking sunlight and impairing photosynthesis. Addressing this issue requires effective water purification methods. Although various physical and chemical techniques such as coagulation, membrane filtration, ozonation, oxidation and biodegradation are employed, they often have limitations. Photocatalysis offers a promising alternative by transforming dye molecules into non-toxic molecules. In this study, methyl violet (MV) dye, soluble in water and used in textiles, paper, paints and printing inks, is chosen due to its toxicity and potential links to human bladder cancer. Therefore, effective removal of this dye from wastewater is crucial [11]. The removal of dyes in the textile waste water is one of the major problems in the industry. So, it is crucial to develop more efficient methods for the degradation of different toxic dyes from the point of view of public health and safety. It is well-known that photocatalyst is a promising potential alternative method for the treatment of wastewater that includes organic pollutants [12].

Several methods are available for synthesizing SnO_2 NPs, including thermal evaporation, combustion route, laser ablation, hydrothermal, solvothermal, chemical precipitation, microemulsion and sol-gel techniques [13,14]. Among these, the hydrothermal method is favoured for its simplicity, cost-effectiveness, minimal environmental impact and energy efficiency. It produces high-purity products with excellent dispersibility and controllable sizes [15]. In this study, pure SnO_2 NPs are synthesized using the hydrothermal method. The effects of calcined temperature and its structural, morphological and optical properties, as well as their electrochemical performance and photocatalytic activity towards methylene violet (MV) dye, are thoroughly investigated.

EXPERIMENTAL

Tin dioxide nanoparticles (SnO_2 NPs) were synthesized using a hydrothermal method. Analytical grade tin(IV) chloride pentahydrate ($SnCl_4 \cdot 5H_2O$) and sodium hydroxide (NaOH), sourced from Sigma-Aldrich (India), were utilized without additional purification.

Preparation of SnO_2 NPs:

$$SnCl_4 + 4NaOH \rightarrow Sn(OH)_4 + 4\,NaCl\downarrow$$
$$Sn(OH)_4 \rightarrow SnO_2 + 2H_2O$$

Pure SnO_2 NPs were synthesized using the hydrothermal method. A 0.1 M solution of $SnCl_4 \cdot 5H_2O$ was prepared by dissolving it in 50 mL of deionized water. Then, 0.2 M NaOH solution was added dropwise to the $SnCl_4$ solution with continuous stirring for 60 min at room temperature using a magnetic stirrer, until a homogeneous mixture was achieved. This homogeneous solution was transferred into a 200 mL Teflon-lined stainless-steel autoclave and heated at 160 ºC for 6 h. Following the reaction, the autoclave was allowed to cool to room temperature. The resulting product was collected, washed several times with deionized water and ethanol to remove impurities and then dried in a hot-air oven at 80 ºC for 3 h. Subsequently, the Sn samples were annealed at three different temperatures for 3 h, designated as Sn5 (500 ºC), Sn6 (600 ºC) and Sn7 (700 ºC).

Photocatalytic activity: The photocatalytic efficacy of the synthesized Sn7 NPs was evaluated for the degradation of MV dye in aqueous solution under sunlight. To optimize dye concentrations, 1 M dye solution was prepared by dissolving MV dye in 500 mL of deionized water. For the degradation test, 2 mg of Sn7 catalyst was introduced into 100 mL of MV dye solution within a 100 mL beaker. The mixture was then exposed to sunlight while being stirred continuously. At 10 min intervals, samples of the dye solution were collected and analyzed using a UV-vis spectrometer. The efficiency of MV dye degradation was calculated using the following formula [16]:

$$D(\%) = \frac{C_o - C_t}{C_o} \times 100 \quad (1)$$

where C_t denotes the dye solution's absorbance after 't' time and C_o is the initial absorbance (t = 0).

Electrochemical measurements: The electrochemical performance of the synthesized Sn7 NPs was evaluated using a three-electrode system, where the Sn7 NPs served as the working electrode. The experiments were conducted at room temperature, with a platinum (Pt) electrode functioning as the auxiliary electrode and an Ag/AgCl electrode serving as the reference electrode. The electrolyte used was a 2 M KOH aqueous solution, which significantly enhance the specific capacitance (C_{sp}) of the material. To prepare the modified working electrode, the doctor blade technique was employed on a nickel plate (1 cm × 1 cm). The electrode active material consisted of a mixture of synthesized SnO_2 NPs, activated carbon and polyvinylidene fluoride (PVDF) binder in the ratio of 85:10:5, respectively. The components were thoroughly ground for 45 min. N-methyl-2-pyrrolidone was added dropwise to the mixture to create a slurry, which was then applied to the surface of the nickel plate and dried in an oven at 80 ºC for 3 h. The electrochemical characterisation was performed using cyclic voltammetry (CV), galvanostatic charge-discharge (GCD) and electrochemical impedance spectroscopy (EIS) techniques on an electrochemical analyzer.

Characterisation: The thermal behaviour of SnO_2 NPs was analyzed using a NETZSCH STA-449F3 Jupiter thermal analyzer. Structural characterisation was carried out *via* X-ray diffraction (XRD) with a XPERT-PRO system employing Cu*K*α radiation (λ = 1.5406 Å), over a 2θ range from 20º to 80º at room temperature. Fourier-transform infrared (FTIR) spectra were recorded using a Perkin-Elmer spectrum RX1 FT-IR spectrometer. Morphological studies were conducted using field emission scanning electron microscopy (FE-SEM, Carl Zeiss Sigma 300) combined with energy-dispersive X-ray spectroscopy (EDS). Optical properties were assessed by diffuse reflectance spectroscopy (DRS) using a UV-2600 spectrophotometer. High-resolution transmission electron microscopy (HRTEM, FEI Tecnai G2 20 Twin) was used to examine the microstructure, morphology and lattice fringe patterns of the samples, with an acceleration voltage set at 200 kV. X-ray photoelectron spectroscopy (XPS, ULVAC-PHI, Model: PH15000) was utilized to analyze the elemental composition and binding states of the SnO_2 NPs.

RESULTS AND DISCUSSION

Thermal studies: The thermogravimetric analysis (TGA) and differential thermal analysis (DTA) curves for the prepared samples are shown in Fig. 1. The TGA data reveal two distinct weight loss phases: an initial reduction of 7.22% between room temperature and 160 ºC, followed by an additional 3.63% weight loss from 160 ºC to 490 ºC. The initial weight loss observed in the TGA curve, coupled with the endothermic peak at 105 ºC in the DTA, is attributed to the desorption of physically adsorbed water [17,18]. The exothermic and endothermic peaks observed between 248 ºC and 294 ºC correspond to the combustion of organic material present on the sample surface. Two significant exothermic peaks at 424.7 ºC and 490 ºC are associated with the carbonisation of organic matter and the removal of water molecules [19]. No further weight loss was detected beyond 490 ºC, indicating the complete formation of SnO_2.

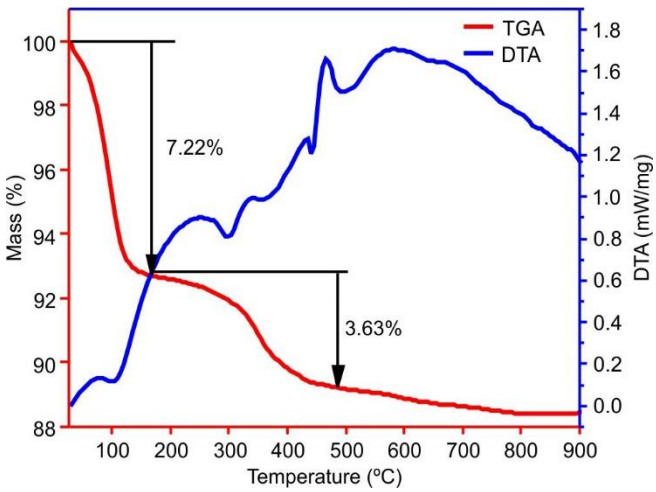

Fig. 1. TG-DTA curves of the as-prepared sample of SnO_2 NPs

Structural studies: The X-ray diffraction (XRD) patterns of the Sn, Sn5, Sn6 and Sn7 samples are shown in Fig. 2. The

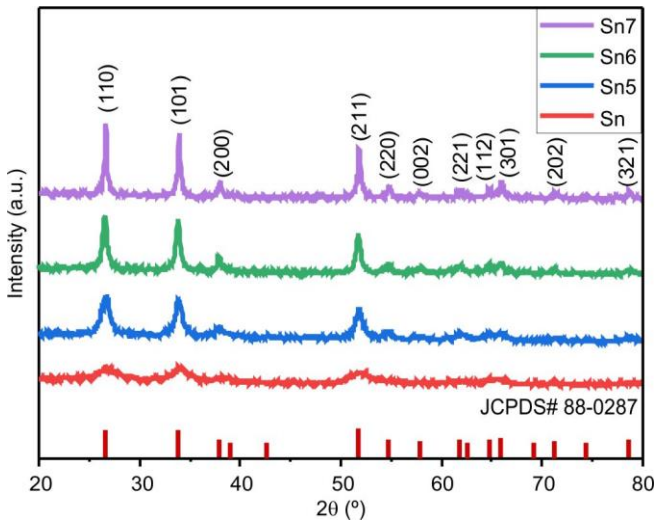

Fig. 2. XRD patterns of SnO_2 NPs

diffraction peaks observed at 26.53º, 33.71º, 37.9º, 51.92º, 54.76º, 62.10º, 64.82º, 66.03º, 71.33º and 78.94º correspond to the (110), (101), (200), (211), (220), (221), (112), (301), (201) and (321) planes, respectively. These peaks are well-matched with the JCPDS data for the tetragonal phase of SnO_2 NPs. The tetragonal structure with space group $P4_2/mnm$ was confirmed according to JCPDS file No. 88-0287 [20]. The peak intensities increased with higher annealing temperatures, with the highest crystallinity observed at 700 ºC. No impurity peaks were detected in the X-ray diffraction patterns. The crystallite size was calculated using the Scherrer's equation [21]:

$$D = \frac{K\lambda}{\beta \cos\theta} \quad (2)$$

where K is a shape factor or constant, λ (α = 1.542 Å; Cu*K*α) is a wavelength, β is a full width at half maximum (FWHM) and θ is a diffraction angle.

The lattice constants a and c for the tetragonal structure of the synthesized nanoparticles were determined using the formula [22]:

$$\frac{1}{d^2} = \frac{h^2 + k^2}{a^2} + \frac{l^2}{c^2} \quad (3)$$

where d is interplanar spacing and *h*, *k* and *l* are the miller indices.

The lattice strain (ε) and dislocation density (δ) were projected *via* the relation [23]:

$$\varepsilon = \frac{\beta}{4\tan\theta} \quad (4)$$

$$\delta = \frac{1}{D^2} \quad (5)$$

The volume of unit cell was calculated by following relation [24]:

$$V = a^2 \cdot c \quad (6)$$

The structural parameters are presented in Table-1. The data reveal that as the calcination temperature increases, the peak intensities in the XRD patterns become sharper and the

TABLE-1
STRUCTURAL PARAMETERS OF SYNTHESIZED SnO_2 NPs

Sample code	Crystallite size (D) (nm)		Lattice parameter (Å)		Microstrain (ε) × 10^{-3} (line^{-2} m^{-4})	Dislocation density (δ) × 10^{-3} (nm^{-2})	Cell volume, V (Å^3)	d-Spacing (Å)
	Debye Scherrer	W-H method	a = b	c				
Sn	8	10	4.738	3.188	1.212	2.032	71.56	2.66671, 1.75538, 1.32508
Sn5	14	12	4.737	3.188	5.875	6.516	71.54	2.64867, 1.76394, 1.32414
Sn6	22	17	4.748	3.179	3.527	2.351	71.69	2.65058, 1.76714, 1.32427
Sn7	28	29	4.732	3.179	2.395	1.335	71.18	2.64103, 1.76458, 1.32124

full width at half-maximum (FWHM) values decrease. This trend indicates that both crystallite size and crystallinity of the SnO_2 NPs improve with higher calcination temperatures [25]. Moreover, the microstrain and dislocation density show an inverse relationship with crystallite size; as the crystallite size increases, both dislocation density and microstrain decrease. Consequently, the microstrain and dislocation density values decline as the calcination temperature of the samples rises [26]. The prominent peaks demonstrated the high purity and crystallinity of the produced materials. The high crystallinity of synthetic materials should increase their electrochemical performance [27].

Rietveld refinement of XRD patterns was performed with an emphasis on the phases and structures of the optimum sample Sn7. The XRD data from Rietveld refinement of the obtained sample were calculated using FULLPROF suite software [28]. The annealed sample of SnO_2 (Sn7) NPs is depicted in Fig. 3. The Rietveld refinement produced the observed patterns (red), calculated patterns (black), difference patterns (blue) and Bragg position (green). The parameters shown in Rietveld refinement for annealed sample are comparable with the calculated values. For this sample, the Rietveld refinement profiles were perfect by simulated as pure single phase of tetragonal SnO_2 structure without any impurities [29]. The difference between calculated patterns and observed patterns is fitted accurately. Table-2 clearly mentions the different parameters obtained from Rietveld refinement for annealed (Sn7) sample. R_{wp} represents the weighted profile parameter R

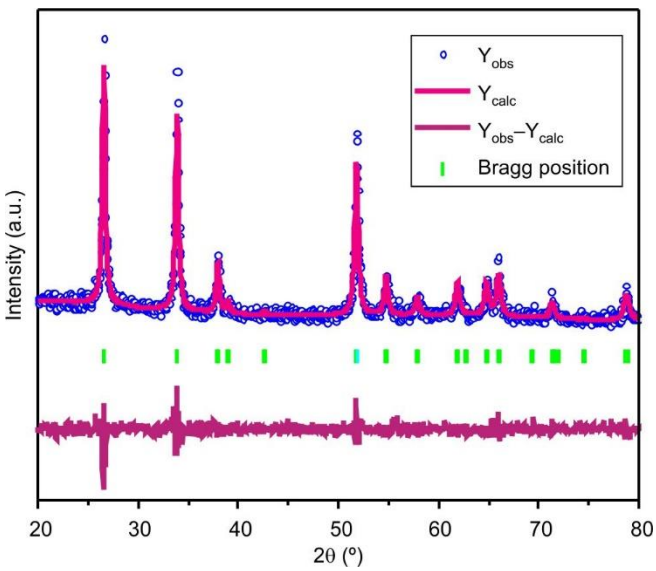

Fig. 3. Rietveld refinement for annealed sample (Sn7) of SnO_2 NPs

TABLE-2
RIETVELD REFINEMENT STRUCTURAL PARAMETERS OF Sn7 NPs

Parameters	Calculated values after refinement
Crystal structure	Tetragonal
Space group	$P4_2/mnm$
Lattice parameter a = b	
a (Å)	4.739
c (Å)	3.186
Unit cell volume (Å^3)	71.51
Average crystallite size	28
R_{wp} %	31.9
R_p %	37.3
χ^2	0.9

value and R_p denotes the unweighted profile parameter and χ^2 represents the goodness of fit of SnO_2 NPs. Sn7 sample is in good agreement with the goodness of fit value.

Using the Williamson Hall method, the crystallite size and lattice strain were also calculated using the following formula [30]:

$$\beta_{hkl}\cos\theta = \left(\frac{k\lambda}{D}\right) + (4\varepsilon\sin\theta) \quad (7)$$

where β is the diffraction peak's full width at half maximum (FWHM); θ is the Bragg angle; k is a shape factor; usually assumed to be 0.9; λ is the X-ray wavelength, D is the size of the crystallite and ε is the lattice strain. Fig. 4 shows the W-H plot, which is derived from the values of 4sin θ that correspond to the βcos θ values of the prepared SnO_2 NPs. Table-1 displays a close agreement between the crystallite size determined using Debye-Scherrer's equation and the crystallite size estimated by the W-H technique.

FTIR studies: The FTIR spectra of the SnO_2 NPs, recorded over the range of 4000 to 400 cm^{-1}, are shown in Fig. 5. The absorption peak around 3455.62 cm^{-1} is attributed to the stretching vibrations of hydroxyl groups, which result from water adsorbed on the surface of the SnO_2 samples. A prominent peak at 1641.60 cm^{-1} corresponds to the bending vibration of the O-H bond, associated with water molecules which are chemically absorbed. The vibration of different types of surface hydroxyl groups was associated with the bands observed in the 1055 cm^{-1} range. The intensity of this O-H bond peak diminishes with increasing annealing temperatures. The peak observed at 644 cm^{-1} is indicative of the Sn-O-Sn bond vibration, confirming the presence of SnO_2 in the nanoparticles. Furthermore, the band at 512 cm^{-1} is attributed to the stretching vibration of the Sn-O bond [31,32].

Microstructural analysis: FESEM has been used to examine the morphology of synthesized SnO_2 NPs. Fig. 6a-f

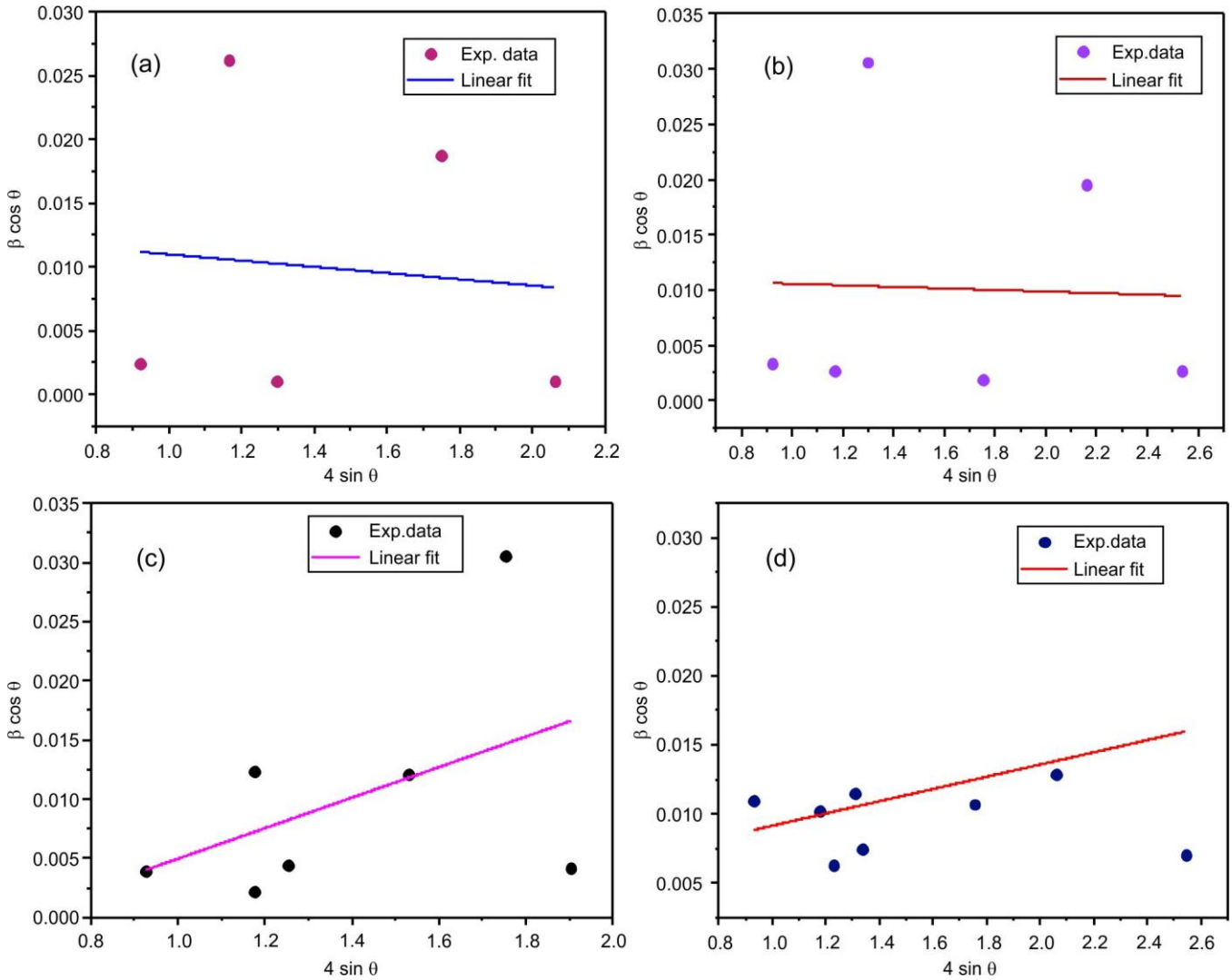

Fig. 4. W-H plots for (a) Sn, (b) Sn5, (c) Sn6 and (d) Sn7 NPs

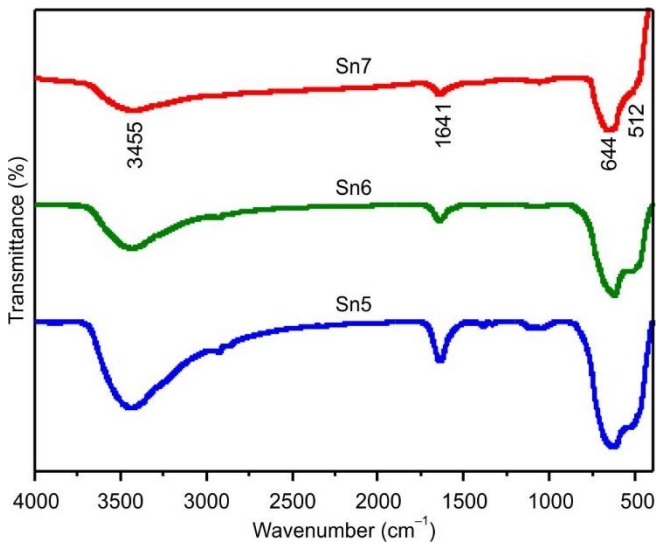

Fig. 5. FT-IR spectra of Sn5, Sn6 and Sn7 NPs

displays the FESEM images and histogram of Sn5, Sn6 and Sn7 NPs. It is observed that most of the particles are equally dispersed, nanosized and agglomerated with spherical in shape [33]. It was evident that the grain sizes increased with annealing temperatures. The smaller crystallite develops closer to the larger one, the particle size is higher than the crystallite size found in XRD. The sizes of Sn5, Sn6 and Sn7 particles were 26, 28 and 33 nm, respectively. The spherical morphology offers an increased specific surface area and a higher density of active sites, thereby promoting the adsorption of dye molecules. This structural advantage directly supports higher photocatalytic activity and contributes to improved charge storage performance in supercapacitors systems [34]. The elemental composition of the Sn7 NPs was determined using EDX, as illustrated in Fig. 6g. The analysis reveals that the NPs consist exclusively of tin and oxygen. The atomic percentages are 36.93% for tin and 63.07% for oxygen. This confirms both the formation of the spherical phase and the high purity of the SnO_2 NPs.

The tetragonal structure of the SnO_2 NPs was confirmed through HR-TEM analysis (Fig. 7a), which is consistent with the XRD results. The particle size distribution histogram (Fig. 7b) indicates an average particle size of 37 nm. The observed interplanar spacings of 0.26, 0.17 and 0.13 nm (Fig. 7c) corres-

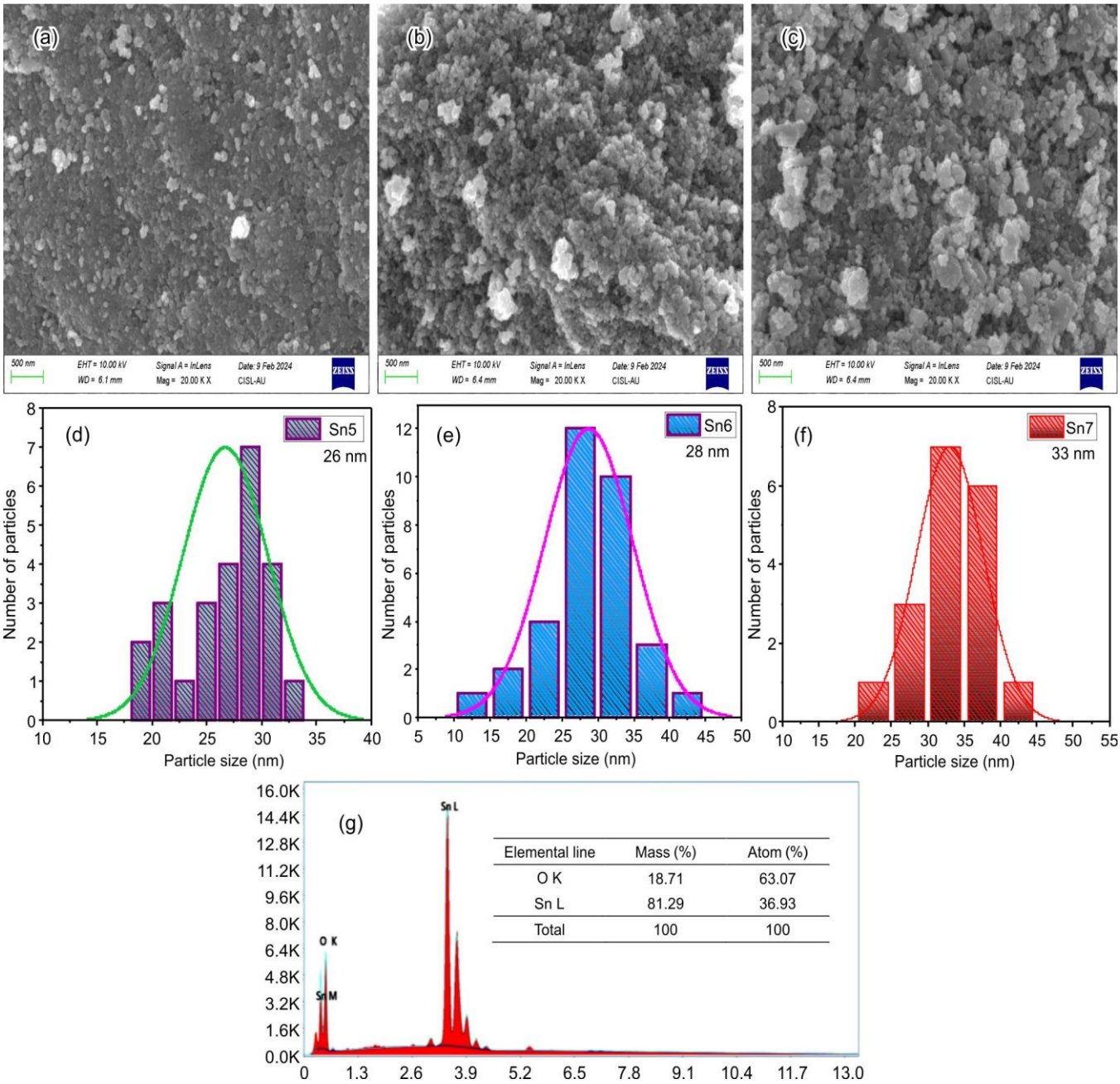

Fig. 6. (a-f) FE-SEM images of Sn5, Sn6 and Sn7 NPs and their particle size distribution respectively; and (g) EDX spectrum of Sn7 NP

pond to the (101), (211) and (112) planes of the tetragonal SnO_2 phase, aligning well with the values derived from XRD analysis [35,36]. SAED pattern, presented in Fig. 7d, displays the characteristic diffraction peaks for the (110), (101), (200), (211) and (112) planes, further confirming the high crystallinity of the SnO_2 NPs and supporting the XRD data [37].

Optical properties: The optical properties of the SnO_2 NPs were assessed using UV-DRS techniques, with the spectra shown in Fig. 8a-b. The reflectance edges for samples annealed at temperatures of Sn5, Sn6 and Sn7 shifted to longer wavelengths, appearing at 278 nm, 281 nm and 282 nm, respectively. The band gap energy of the material was calculated using the Kubelka-Munk function, as outlined by the following relation [38]:

$$F(R) = \frac{(1-R)^2}{2R} \quad (8)$$

where F(R) is the Kubelka-Munk function which corresponds to absorption coefficient and R is the reflectance of the sample. The optical band gap was determined by extrapolating the linear portion of the plot of $(F(R))^2$ *versus* photon energy ($h\nu$). The measured band gap values were 3.73 eV, 3.62 eV and 3.43 eV for the Sn5, Sn6 and Sn7 NPs, respectively. This decrease in band gap with increasing annealing temperature and crystallite size suggests an inverse relationship between the band gap and crystallite size. The observed red shift in the band gap of these SnO_2 NPs further supports this finding [39,40].

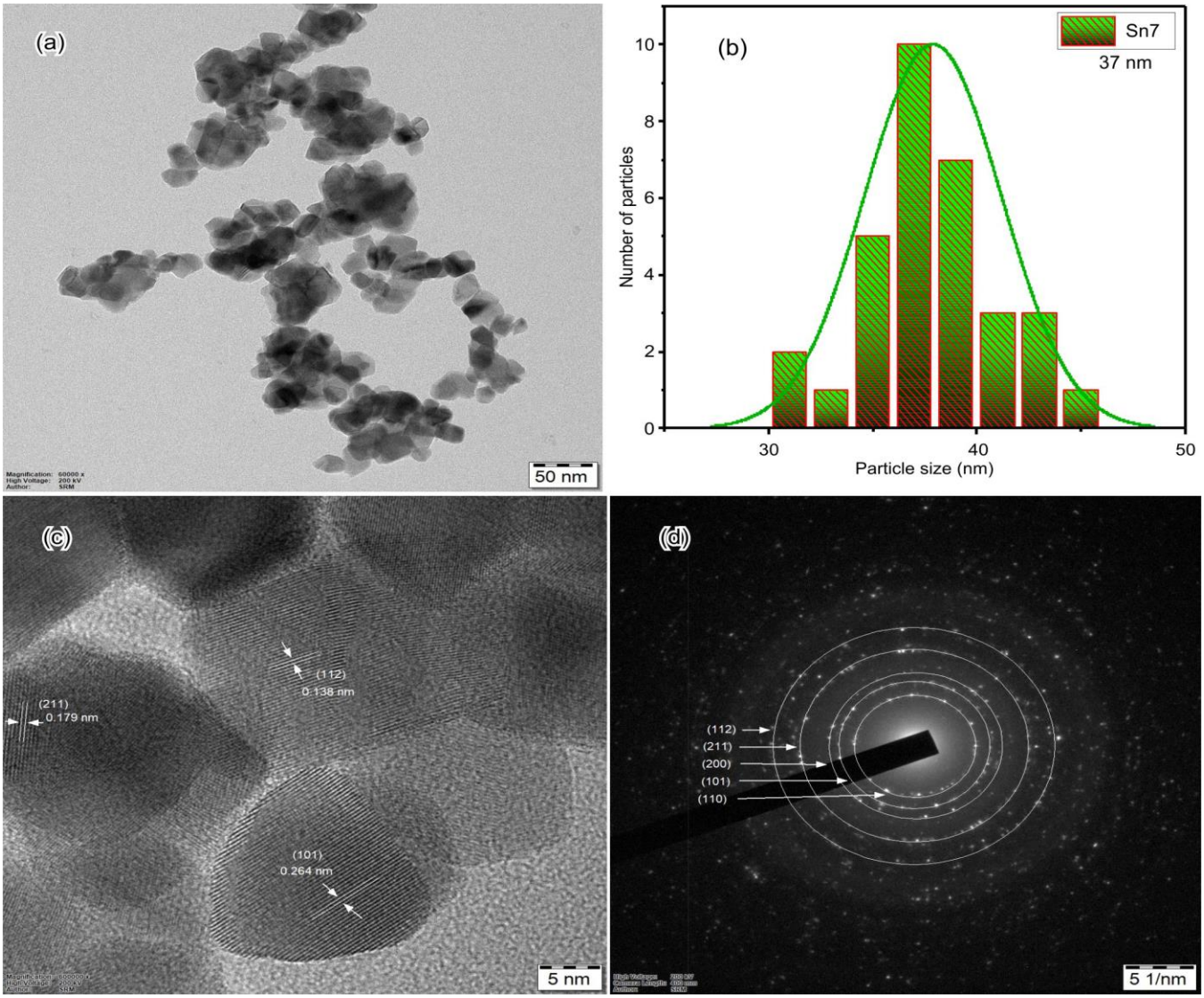

Fig. 7. (a) HR-TEM image, (b) particle size distribution, (c) fringe pattern and (d) SAED pattern of Sn7 NP

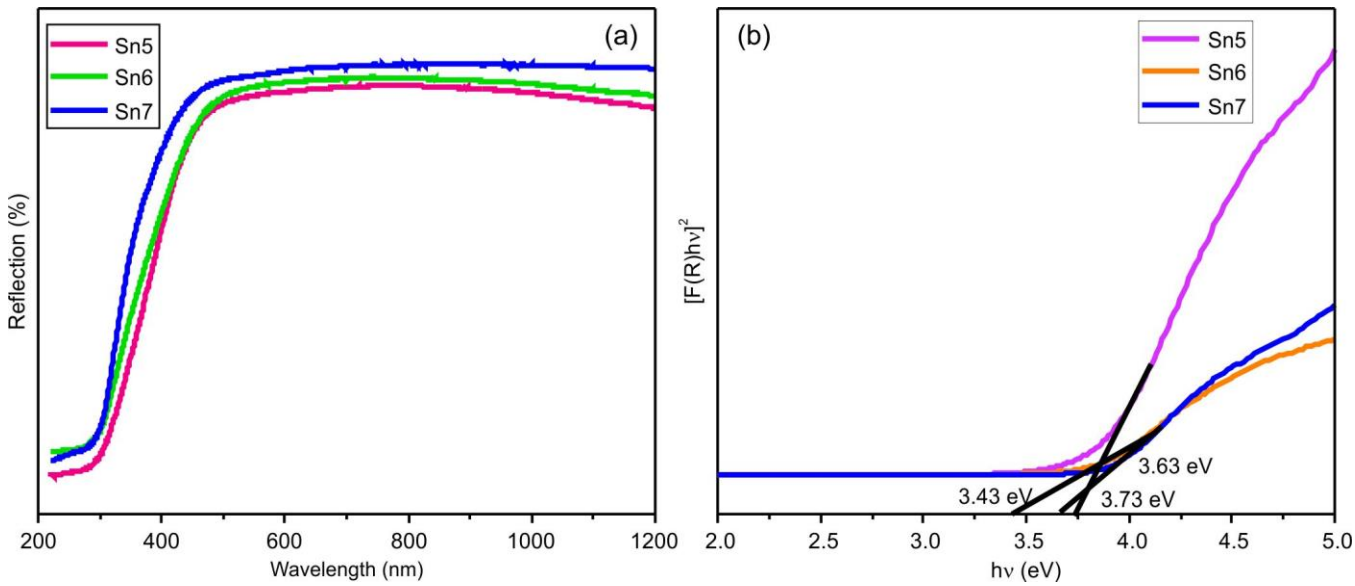

Fig. 8. (a) Reflectance spectra, (b) K-M plot of synthesized SnO_2 NPs

XPS studies: X-ray photoelectron spectroscopy (XPS) was employed to elucidate the elemental composition and chemical states within the Sn7 NPs. This technique provides insights into the electronic structure of the elements present in the sample. Fig. 9a-c displays the XPS spectra for Sn 3d and O 1s regions, confirming the presence of Sn and O. The C 1s peak at 286.1 eV was used as the reference for binding energy calibration in Fig. 9a [41]. Fig 9b revealed the Sn $3d_{5/2}$ and Sn $3d_{3/2}$ peaks are located at binding energies of 487.3 eV and 495.7 eV, respectively, which are characteristic of the Sn^{4+} oxidation state [42]. In Fig. 9c, the O 1s peak observed at 530.8 eV indicates that the oxygen atoms are present as O^{2-} species [43].

Photocatalytic activity: Fig. 10a shows the changes in the absorbance spectrum of methyl violet (MV) dye at 581 nm under sunlight irradiation in the presence of Sn7 catalyst over different time intervals. The characteristic absorption peak of MV dye molecules diminishes rapidly with sunlight exposure, disappearing completely after 70 min, reflecting an 85% degradation, as illustrated in Fig. 10b. This indicates effective decolourisation of the MV dye. The absorption *versus* time plot in Fig. 10c further illustrates the degradation process of MV dye molecules. Furthermore, the kinetics of MV degradation using SnO_2 NPs were analyzed using the Langmuir-Hinshelwood kinetic model, as described by the following relation [44].

$$\ln\frac{C_o}{C_t} = kt \quad (9)$$

where C_o is the initial MV absorbance; C_t is the final MV absorbance; and k is the rate constant. The rate constant (k) can be obtained from the slope of the curve drawn between ln (C_o/C_t) and time, as shown in Fig. 10c. The photo degradation rate (MV + SnO_2) at 85% degradation was 2.72×10^{-2} min^{-1}.

Mechanism of photocatalytic activity: Fig. 11 shows the schematic diagram of photocatalytic mechanism of SnO_2 NPs. When the Sn7 catalyst is exposed to sunlight, it generates electron-hole pairs, with electrons being excited to the conduction band and holes remaining in the valence band. The photogenerated holes (h^+) then oxidize water (H_2O) to produce hydroxyl radicals ($^\bullet OH$), which are highly reactive and play a crucial role in the degradation of pollutants by converting them into carbon dioxide (CO_2) and water (H_2O). Meanwhile, electrons can react with molecular oxygen to form superoxide radicals ($^\bullet O_2^-$). The methyl violet dye undergoes degradation through direct oxidation by these hydroxyl radicals ($^\bullet OH$) and superoxide radicals ($^\bullet O_2^-$). The degradation mechanism of MV on the Sn7 catalyst is outlined as follows [45]:

$$SnO_2 + h\nu \rightarrow e^-_{CB} + h^+_{VB} \quad (10)$$

$$h^+_{VB} + H_2O_{ads} \rightarrow {}^\bullet OH + H^+ \quad (11)$$

$$h^+_{VB} + OH^-_{ads} \rightarrow {}^\bullet OH \quad (12)$$

$$e^-_{CB} + O_2 \rightarrow O_2^{\bullet -} \quad (13)$$

$$OH + Dye + O_2 \rightarrow \text{Degradation product} \quad (14)$$

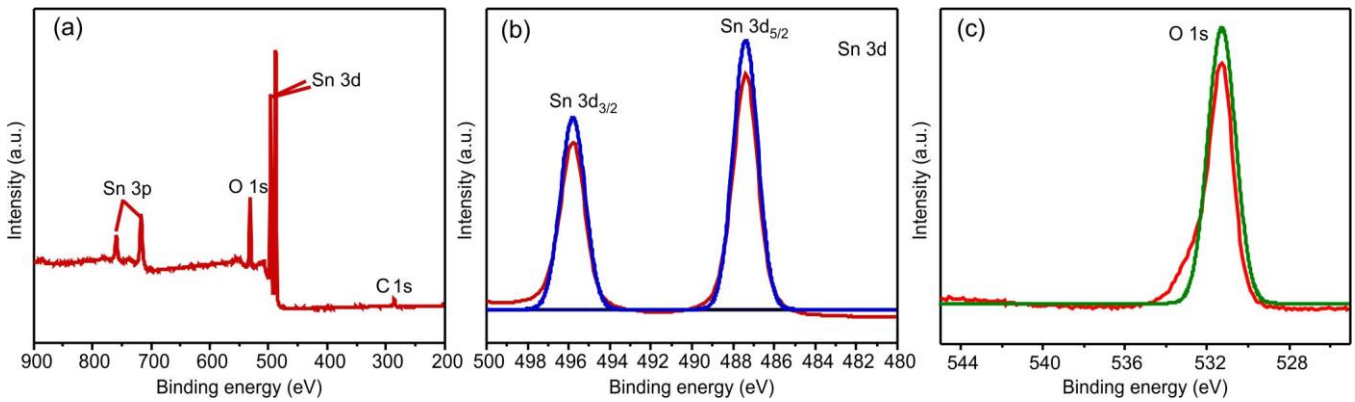

Fig. 9. XPS spectra of (a) SnO_2, (b) Sn 3d, (c) O1s of Sn7 samples

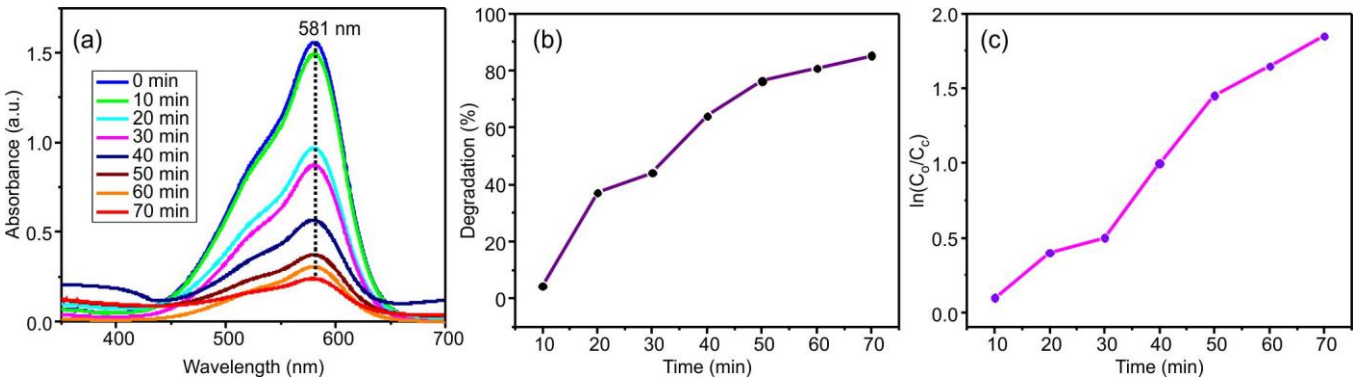

Fig. 10. (a) Photocatalytic degradation of MV, (b) degradation efficiency of MV for different degradation times, (c) rate constant plot of MV

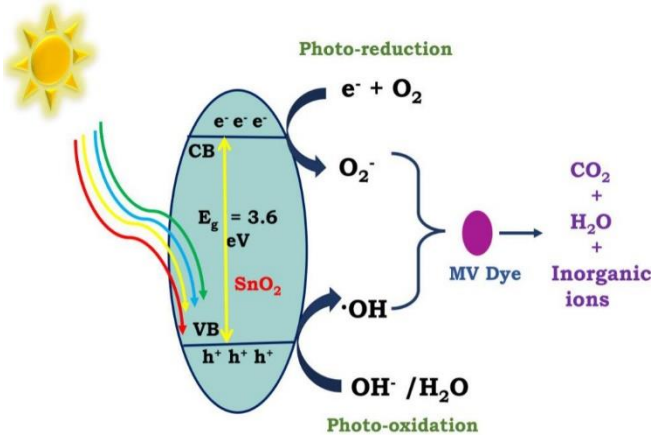

Fig. 11. Possible photocatalytic mechanism of SnO_2 NPs on MV dye under natural light

Electrochemical performance: The electrochemical performance of the synthesized SnO_2 NPs was evaluated using CV, GCD, EIS and cyclic stability. Fig. 12a displays the CV curves of SnO_2 NPs across a potential range of 0 to 0.4 V, recorded at various scan rates: 5, 10, 15, 20, 25, 50, 75 and 100 mV s^{-1}, with 2M KOH serving as the electrolyte. The CV curves reveal distinct redox peaks, indicative of the pseudocapacitive behaviour of the electrodes, which arises from the reversible Faradaic redox reactions. As the scan rate increases, both the peak current density and its position within the redox potential shift upwards, suggesting enhanced ion diffusion and adsorption within the electrodes [46]. Despite varying scan rates, the CV curves for the Sn7 electrode consistently maintain a similar shape, demonstrating stable electrochemical performance across the different rates. The specific capacitance (C_{sp}) of the Sn7 electrode was derived from the CV curves using eqn. 15 [47]:

$$C_{sp} = \frac{Q}{m\Delta V} \quad (15)$$

where C_{sp} is the specific capacitance; Q is the anodic and cathodic charges on each scan; m is the mass of the active material (mg) in electrode; and ΔV is the scan rate (mV s^{-1}). In CV measurements, the specific capacitance is derived from the integrated area of the CV curve. For bare Sn7 electrode,

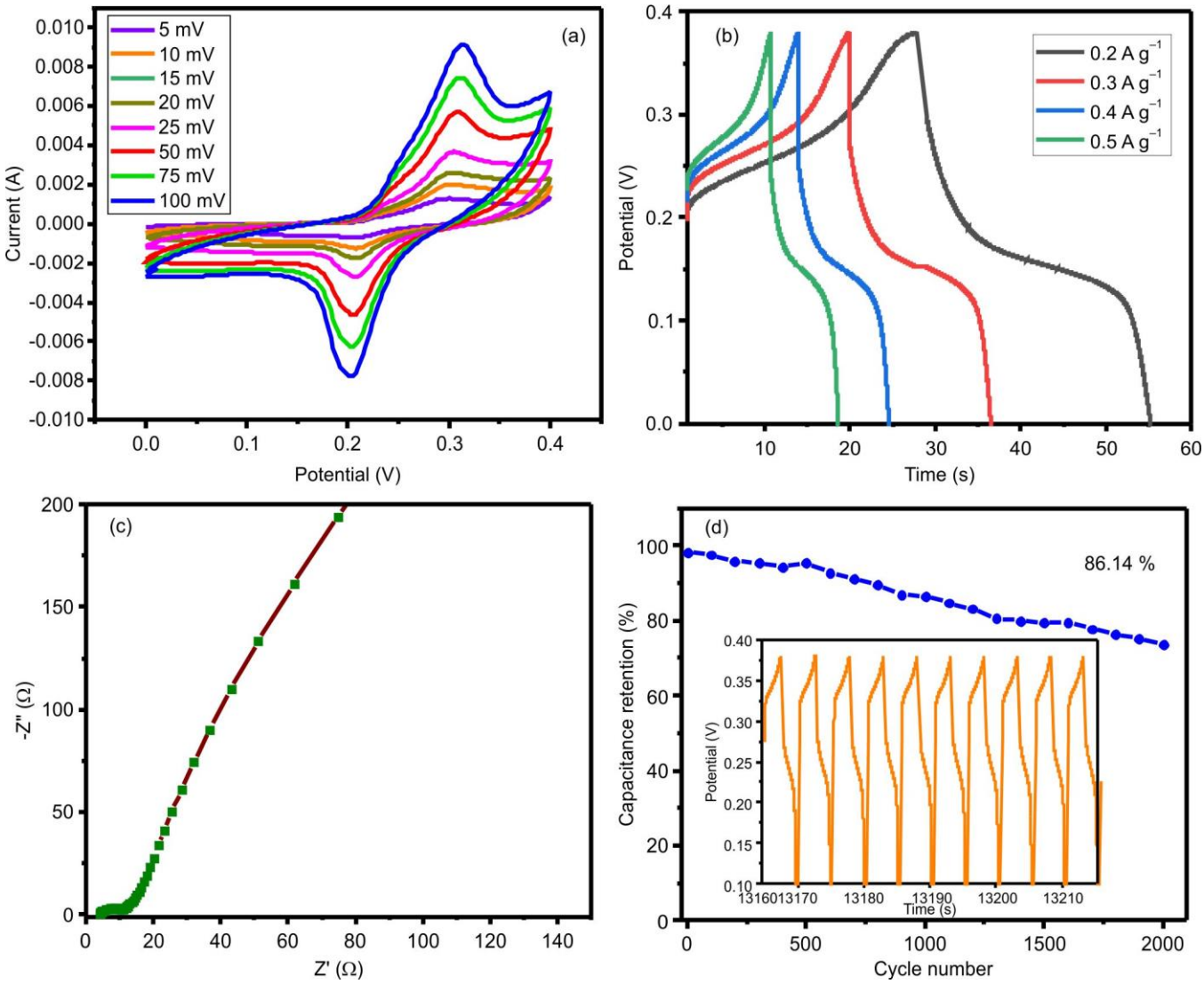

Fig. 12. CV curves (a), GCD curves (b), EIS plots (c) and cyclic stability of Sn7 NPs (d)

TABLE-3
ELECTROCHEMICAL AND PHOTOCATALYTIC (METHYL VIOLET) PROPERTIES OF SnO_2 NANOPARTICLES REPORTED IN PREVIOUS LITERATURE

Synthesis method	Electrolyte	Capacitance (F g^{-1})	Photocatalytic (methyl violet dye) application	Ref.
Co-precipitate	2 M KOH	197	–	[6]
Hydrothermal method (160 ºC for 12 h)	6 M KOH	87	80% for 120 min	[11]
Chemical precipitate	1 M KCl	176	–	[47]
Chemical route	0.5 Na_2SO_4	66	–	[49]
Hydrothermal method (180 ºC for 8 h)	1 M Na_2SO_4	187	–	[50]
Chemical precipitation	–	–	98.5% for 240 min	[51]
Hydrothermal method (130 ºC for 2 h)	1 M KOH	35.07	–	[52]
Green synthesis	1 M KCl	154.33	–	[53]
Soft-chemical approach	2 M KOH	79.13	–	[54]
Hydrothermal method	1 M KOH	187	–	[55]
Hydrothermal method (160 ºC for 6 h)	2 M KOH	213	85% for 70 min	Present work

the specific capacitance values at various scan rates 5, 10, 15, 20, 25, 50, 75 and 100 mV s^{-1} are 213, 179, 155, 132, 126, 90, 75 and 66 F g^{-1}, respectively. The observed decrease in specific capacitance with increasing scan rates is attributed to diffusion limitations. Specifically, as the scan rate increases from 5 mV s^{-1} to 100 mV s^{-1}, the capacitance of Sn7 electrode material diminishes. This reduction is primarily due to the limited ability of protons to diffuse into the interior of the SnO_2 matrix at higher scan rates, which restricts their access to the inner regions of the electrode material. Consequently, the maximum specific capacitance of 213 F g^{-1} is observed at a scan rate of 5 mV s^{-1}. The decline in capacitance at higher scan rates can be explained by two mechanisms: first, the intercalation or deintercalation of protons, which diminishes as the scan rate increases due to the limited proton access; and second, the diffusion effect, where protons struggle to penetrate the electrode material, thereby reducing the specific capacitance [11].

CV provides fundamental insights into the oxidation and reduction processes of molecular species, offering a measure of total charge or specific capacitance. In contrast, GCD testing assesses the discharge capabilities of electrode, further informing specific capacitance calculations. Fig. 12b illustrates the GCD curves for the synthesized SnO_2 at various current densities of 0.2, 0.3, 0.4 and 0.5 A g^{-1}, within a potential range of 0 V to 0.38 V in a 2 M KOH electrolyte. The specific capacitance of the SnO_2 electrode is calculated from the GCD curve according to the eqn. 16 [48]:

$$C_{sp} = \frac{i\Delta t}{m\Delta V} \quad (16)$$

where Δt is the discharge time (s); i is the charge-discharge current (A); ΔV is the potential change during the discharge; and m is the mass of active material in Sn7 electrode. The specific capacitance values of the Sn7 electrode, derived from the charge-discharge curves, are 271, 250, 235 and 213 F g^{-1} at current densities of 0.2, 0.3, 0.4 and 0.5 A g^{-1}, respectively. The observed decrease in specific capacitance with increasing current density is attributed to the restricted movement of electrolyte ions within the electrode material (Fig. 12b). The specific capacitance is computed from the discharge curves and the relationship between capacitance and energy density is illustrated in the corresponding graph. The highest specific capacitance of 271 F g^{-1} is recorded for the SnO_2 electrode at a current density of 0.2 A g^{-1}. Table-3 shows the comparison of electrochemical and photocatalytic degradation of SnO_2 NPs reported in previous literature.

EIS was employed to assess the electrical and conductive properties of the prepared Sn7 electrode. The impedance measurements were conducted across a frequency range from 100 kHz to 0.1 Hz under open circuit conditions. The Nyquist plots for the Sn7 electrode are presented in Fig. 12c. The plots reveal a semicircle in the high-frequency region, indicating charge transfer resistance associated with charge diffusion and a straight line in the low-frequency region, which signifies ideal capacitive behaviour. The solution resistance was measured at 0.75 Ω. These EIS results suggest that SnO_2 exhibits favourable capacitive properties, consistent with the findings from CV and GCD analyses.

Besides, the stability of Sn7 electrode is crucial for energy storage applications. To evaluate this, Sn7 electrode was subjected to cyclic stability testing at a current density of 5 A g^{-1} for up to 2000 cycles (Fig. 12d). This electrode demonstrated approximately 86.14% stability over 2000 cycles. This high stability is attributed to the robust crystalline structure of the SnO_2 NPs material, which helps maintain the integrity of the electrolyte channels and prevents material leaching from the electrode surface [56-58]. The enhanced cyclic retention confirms the suitability of Sn7 electrode for energy storage application.

Conclusion

Briefly, pure SnO_2 NPs were successfully synthesized using hydrothermal method. FTIR spectral results validated the formation of metal oxides. FESEM images indicated the presence of a spherical agglomerated morphology, while complementary HRTEM and XRD analyses confirmed the tetragonal phase structure. The optical band gaps of the SnO_2 NPs were determined to be 3.73, 3.62 and 3.43 eV using UV-DRS analysis. The Sn7 electrode exhibited remarkable electrochemical performance, delivering a specific capacitance of 271 F g^{-1} at a current density of 0.2 A g^{-1}. Furthermore, it demonstrated excellent cycling stability, retaining 86.14% of its initial capacitance after 2000 continuous charge–discharge cycles. The Sn7 catalyst degraded 85% of MV dye within 70 min, highlighting its strong photocatalytic activity. These

findings indicate that SnO_2 NPs have significant potential in both energy storage applications such as supercapacitors and in industrial processes for the degradation of organic pollutants.

CONFLICT OF INTEREST

The authors declare that there is no conflict of interests regarding the publication of this article.

DECLARATION OF AI-ASSISTED TECHNOLOGIES

During the preparation of this manuscript, the authors used an AI-assisted tool(s) to improve the language. The authors reviewed and edited the content and take full responsibility for the published work.

REFERENCES

1. R. Malik, V.K. Tomer, S. Duhan, S.P. Nehra and P.S. Rana, *Energy and Environment Focus*, **4**, 340 (2015); https://doi.org/10.1166/eef.2015.1182.
2. X. Meng, M. Zhou, X. Li, J. Yao, F. Liu, H. He, P. Xiao and Y. Zhang, *Electrochim. Acta*, **109**, 20 (2013); https://doi.org/10.1016/j.electacta.2013.07.052
3. S. Ragupathy and T. Sathya, *J. Mater. Sci. Mater. Electron.*, **29**, 8710 (2018); https://doi.org/10.1007/s10854-018-8886-6
4. K. Dhinakar, T. Selvalakshmi, S.M. Sundar and A. Chandra Bose, *J. Mater. Sci. Mater. Electron.*, **27**, 5818 (2016); https://doi.org/10.1007/s10854-016-4497-2
5. S. Suthakaran, S. Dhanapandian, N. Krishnakumar and N. Ponpandian, *J. Mater. Sci. Mater. Electron.*, **30**, 13174 (2019); https://doi.org/10.1007/s10854-019-01681-7
6. S. Asaithambi, P. Sakthivel, M. Karuppaiah, K. Balamurugan, G.U. Sankar, R. Yuvakkumar, M. Thambidurai and G. Ravi, *J. Energy Storage*, **31**, 101530 (2020); https://doi.org/10.1016/j.est.2020.101530
7. J.-Z. Su, X.-F. Wu, Y.-N. Cui, H. Wang, L.-J. Song, J.-L. Shang, Y.-M. Shi, Z.-D. Wang, C.-Y. Zhang and Y.-Q. Zuo, *J. Mater. Sci. Mater. Electron.*, **31**, 1585 (2020); https://doi.org/10.1007/s10854-019-02675-1
8. S.P. Lim, N.M. Huang and H.N. Lim, *Ceram. Int.*, **39**, 6647 (2013); https://doi.org/10.1016/j.ceramint.2013.01.102
9. X. Wang, Y. Yang, P. He, F. Zhang, J. Tang, Z. Guo and R. Que, *J. Mater. Sci. Mater. Electron.*, **31**, 1355 (2020); https://doi.org/10.1007/s10854-019-02649-3
10. A. Murugan, V. Siva, A. Shameem, S.A. Bahadur, S. Sasikumar and N. Nallamuthu, *J. Energy Storage*, **28**, 101194 (2020); https://doi.org/10.1016/j.est.2020.101194
11. S. Suthakaran, S. Dhanapandian, N. Krishnakumar and N. Ponpandian, *Mater. Res. Express*, **6**, 0850i3 (2019); https://doi.org/10.1088/2053-1591/ab29c2.
12. A.P. Periyasamy, *Sustainability*, **16**, 495 (2024); https://doi.org/10.3390/su16020495
13. Y. Li, R. Peng, X. Xiu, X. Zheng, X. Zhang and G. Zhai, *Superlattices Microstruct.*, **50**, 511 (2011); https://doi.org/10.1016/j.spmi.2011.08.013
14. G.H. Patel, S.H. Chaki, R.M. Kannaujiya, Z.R. Parekh, A.B. Hirpara, A.J. Khimani and M.P. Deshpande, *Physica B*, **613**, 412987 (2021); https://doi.org/10.1016/j.physb.2021.412987
15. M. Wang, Y. Gao, L. Dai, C. Cao and X. Guo, *J. Solid State Chem.*, **189**, 49 (2012); https://doi.org/10.1016/j.jssc.2012.01.021
16. V. Vinosel, S. Anand, M.A. Janifer, S. Pauline, S. Dhanavel, P. Praveena and A. Stephen, *J. Mater. Sci. Mater. Electron.*, **30**, 9663 (2019); https://doi.org/10.1007/s10854-019-01300-5
17. Y. Wang, C. Ma, X. Sun and H. Li, *Nanotechnology*, **13**, 565 (2002); https://doi.org/10.1088/0957-4484/13/5/304
18. N.L. Myadam, D.Y. Nadargi, J.D. Nadargi and M.G. Chaskar, *J. Sol-Gel Sci. Technol.*, **96**, 56 (2020); https://doi.org/10.1007/s10971-020-05377-x
19. J. Sheng, H. Tong, H. Xu and C. Tang, *Catal. Surv. Asia*, **20**, 167 (2016); https://doi.org/10.1007/s10563-016-9217-7
20. K. Prakash, P. Senthil Kumar, S. Pandiaraj, K. Saravanakumar and S. Karuthapandian, *J. Exp. Nanosci.*, **11**, 1138 (2016); https://doi.org/10.1080/17458080.2016.1188222
21. G. Elango and S.M. Roopan, *J. Photochem. Photobiol. B*, **155**, 34 (2016); https://doi.org/10.1016/j.jphotobiol.2015.12.010
22. A. Ayeshamariam, V.S. Vidhya, S. Sivaranjani, M. Bououdina, R. Perumalsamy and M. Jayachandran, *J. Nanoelectron. Optoelectron.*, **8**, 273 (2013); https://doi.org/10.1166/jno.2013.1471.
23. A. Priyadharsini, M. Saravanakumar, J. Suryakanth, S. Pavithra, A. Sakunthala, S. Kavitha, V. Rukkumani and G. Ananthakumari, *Bull. Mater. Sci.*, **46**, 205 (2023); https://doi.org/10.1007/s12034-023-03039-6
24. K.C. Suresh, S. Surendhiran, P. Manoj Kumar, E. Ranjth Kumar, Y.A.S. Khadar and A. Balamurugan, *SN Appl. Sci.*, **2**, 1735 (2020); https://doi.org/10.1007/s42452-020-03534-z
25. S. Naz, I. Javid, S. Konwar, K. Surana, P.K. Singh, M. Sahni and B. Bhattacharya, *SN Appl. Sci.*, **2**, 975 (2020); https://doi.org/10.1007/s42452-020-2812-2
26. A. Abdelkrim, S. Rahmane, O. Abdelouahab, A. Hafida and K. Nabila, *Chin. Phys. B*, **25**, 046801 (2016); https://doi.org/10.1088/1674-1056/25/4/046801
27. E. Ullah, M.Z.U. Shah, S.A. Ahmad, M. Arif, M.I. Khan, M. Hou, S. Guo, A. Shah and M. Sajjad, *Mater. Today Commun.*, **37**, 106889 (2023); https://doi.org/10.1016/j.mtcomm.2023.106889
28. S.M. Yakout, *J. Mater. Sci. Mater. Electron.*, **30**, 17053 (2019); https://doi.org/10.1007/s10854-019-02052-y
29. K. Rajwali and M.-H. Fang, *Chin. Phys. B*, **24**, 127803 (2015); https://doi.org/10.1088/1674-1056/24/12/127803
30. R. Rajan and R.E. Vizhi, *J. Mater. Sci. Mater. Electron.*, **32**, 12716 (2021); https://doi.org/10.1007/s10854-021-05906-6
31. Z. Li, W. Shen, X. Zhang, L. Fang and X. Zu, *Colloids Surf. A Physicochem. Eng. Asp.*, **327**, 17 (2008); https://doi.org/10.1016/j.colsurfa.2008.05.043
32. M.A. Gondal, Q.A. Drmosh and T.A. Saleh, *Appl. Surf. Sci.*, **256**, 7067 (2010); https://doi.org/10.1016/j.apsusc.2010.05.027
33. E.C. Nwanna, P.E. Imoisili and T.-C. Jen, *J. King Saud Univ. Sci.*, **34**, 102123 (2022); https://doi.org/10.1016/j.jksus.2022.102123
34. S. Suthakaran, S. Dhanapandian, N. Krishnakumar and N. Ponpandian, *J. Phys. Chem. Solids*, **141**, 109407 (2020); https://doi.org/10.1016/j.jpcs.2020.109407
35. L. Cheng, S.Y. Ma, X.B. Li, J. Luo, W.Q. Li, F.M. Li, Y.Z. Mao, T.T. Wang and Y.F. Li, *Sens. Actuators B Chem.*, **200**, 181 (2014); https://doi.org/10.1016/j.snb.2014.04.063
36. Y. Chen, H. Qin, Y. Cao, H. Zhang and J. Hu, *Sensors*, **18**, 3425 (2018); https://doi.org/10.3390/s18103425
37. G.E. Patil, D.D. Kajale, V.B. Gaikwad and G.H. Jain, *Int. Nano Lett.*, **2**, 17 (2012); https://doi.org/10.1186/2228-5326-2-17
38. H. Zhu, D. Yang, G. Yu, H. Zhang and K. Yao, *Nanotechnology*, **17**, 2386 (2006); https://doi.org/10.1088/0957-4484/17/9/052
39. P. Chetri and A. Choudhury, *Physica E*, **47**, 257 (2013); https://doi.org/10.1016/j.physe.2012.11.011
40. N. Talebian and F. Jafarinezhad, *Ceram. Int.*, **39**, 8311 (2013); https://doi.org/10.1016/j.ceramint.2013.03.101
41. J. Saddique, H. Shen, J. Ge, X. Huo, N. Rahman, M. Mushtaq, K. Althubeiti and H. Al-Shehri, *Materials*, **15**, 2475 (2022); https://doi.org/10.3390/ma15072475
42. A. Elci, O. Demirtas, I.M. Ozturk, A. Bek and E. Nalbant-Esenturk, *J. Mater. Sci.*, **53**, 16345 (2018); https://doi.org/10.1007/s10853-018-2792-4
43. F. Davar, M. Salavati-Niasari and Z. Fereshteh, *J. Alloys Compd.*, **496**, 638 (2010); https://doi.org/10.1016/j.jallcom.2010.02.152

44. S.K. Tammina, B.K. Mandal and N.K. Kadiyala, *Environ. Nanotechnol. Monit. Manag.*, **10**, 339 (2018); https://doi.org/10.1016/j.enmm.2018.07.006
45. S. Sonia, S. Poongodi, P.S. Kumar, D. Mangalaraj, N. Ponpandian and C. Viswanathan, *Mater. Sci. Semicond. Process.*, **30**, 585 (2015); https://doi.org/10.1016/j.mssp.2014.10.012
46. S. Asaithambi, P. Sakthivel, M. Karuppaiah, K. Balamurugan, R. Yuvakkumar, M. Thambidurai and G. Ravi, *J. Alloys Compd.*, **853**, 157060 (2021); https://doi.org/10.1016/j.jallcom.2020.157060
47. E. Manikandan, J.C. Kannan, V. Devabharathi, S. Pushpa and N. Ahmad Mala, *Mater. Today Proc.*, **80**, 1591 (2023); https://doi.org/10.1016/j.matpr.2023.01.395
48. J. Jayachandiran, J. Yesuraj, M. Arivanandhan, B. Muthuraaman, R. Jayavel and D. Nedumaran, *RSC Adv.*, **11**, 856 (2021); https://doi.org/10.1039/D0RA10137K
49. S.N. Pusawale, P.R. Deshmukh and C.D. Lokhande, *Appl. Surf. Sci.*, **257**, 9498 (2011); https://doi.org/10.1016/j.apsusc.2011.06.043
50. Y. Liu, Y. Jiao, Z. Zhang, F. Qu, A. Umar and X. Wu, *ACS Appl. Mater. Interfaces*, **6**, 2174 (2014); https://doi.org/10.1021/am405301v
51. A. Bhattacharjee, M. Ahmaruzzaman and T. Sinha, *Spectrochim. Acta A Mol. Biomol. Spectrosc.*, **136**, 751 (2015); https://doi.org/10.1016/j.saa.2014.09.092
52. S.K. Godlaveeti, A.R. Somala, S.S. Sana, M. Ouladsmane, A.A. Ghfar and R.R. Nagireddy, *J. Cluster Sci.*, **33**, 1635 (2022); https://doi.org/10.1007/s10876-021-02092-7
53. S. Amuthameena, K. Dhayalini, B. Balraj, C. Siva and N. Senthilkumar, *Inorg. Chem. Commun.*, **131**, 108803 (2021); https://doi.org/10.1016/j.inoche.2021.108803
54. B. Babu, B. Talluri, T.R. Gurugubelli, J. Kim and K. Yoo, *Chemosphere*, **286**, 131577 (2022); https://doi.org/10.1016/j.chemosphere.2021.131577
55. B. Padmaja, S. Dhanapandian, S. Suthakaran, K. Ashokkumar and N. Krishnakumar, *Inorg. Chem. Commun.*, **149**, 110363 (2023); https://doi.org/10.1016/j.inoche.2022.110363
56. F.S. Omar, A. Numan, N. Duraisamy, M.M. Ramly, R. K and R. S, *Electrochim. Acta*, **227**, 41 (2017); https://doi.org/10.1016/j.electacta.2017.01.006
57. N. Duraisamy, A. Numan, S.O. Fatin, K. Ramesh and S. Ramesh, *J. Colloid Interface Sci.*, **471**, 136 (2016); https://doi.org/10.1016/j.jcis.2016.03.013
58. N. Duraisamy, K. Kandiah, R. Rajendran and G. Dhanaraj, *Res. Chem. Intermed.*, **44**, 5653 (2018); https://doi.org/10.1007/s11164-018-3446-5